

## Particle Image Velocimetry Measurements on a Generic Submarine Hull Form

C. Kumar, P. Manovski and M. Giacobello

Defence Science and Technology Organisation  
506 Lorimer St., Fishermans Bend, Victoria 3207, Melbourne, Australia

### Abstract

Particle Image Velocimetry (PIV) measurements were conducted on the Defence Science and Technology Organisation (DSTO) generic submarine hull form. The hull form comprises an axisymmetric body, with large casing and fin and an X-form rudder arrangement. Testing was conducted at the DSTO Low Speed Wind Tunnel (LSWT) on a 1.35 m model at 30 m/s, yielding a Reynolds number, based on the model length, of  $Re = 2.7 \times 10^6$ . PIV measurements consisting of ensemble averaged flow fields and turbulence statistics were gathered at side slip angles of  $\beta = 0^\circ$  and  $\beta = 10^\circ$ . Combined with other experimental data, the PIV results will provide insight into the vortical systems generated around a submarine. The generated data is part of a comprehensive experimental database that can be referred to for future Computational Fluid Dynamics (CFD) validation.

### Introduction

Limited studies exist in open literature dealing with flows over diesel electric submarine geometries. Most studies refer to the DARPA SUBOFF model [6, 7], which is based on a generic axisymmetric hull, without casing, and a cruciform rudder arrangement. The SUBOFF model is representative of a nuclear submarine. The DSTO generic submarine hull form was developed to provide an equivalent representation for a diesel electric submarine, with large casing, fin, and an X-form rudder arrangement. The DSTO hull form is based on the work of Joubert [8, 9] and comprises of an axisymmetric body with a length to diameter ratio of 7.3. The nose shape was designed with the aim of maintaining natural laminar flow over the bow. The after-body is based on a number of successive conical sections, shown to produce acceptable flow into the propeller plane. The aim of this study is to provide a comprehensive experimental database for the DSTO hull form. This database will provide insights into the vortical systems generated around a submarine and will be referred to for CFD validation.

For a submarine on a straight course the boundary layer rapidly thickens as it moves over the length of the boat. Encountering the fin, the flow diverts into two counter-rotating longitudinal horse-shoe vortices. Tip vortices form at the fin-cap. Additional counter-rotating horse-shoe vortices are produced across the diving plane and stern control surfaces. These vortices interact with the thickening boundary layer and introduce non-uniformities in the flow field [5]. These flow structures become more pronounced for a manoeuvring submarine. Figure 1 highlights the system of vortices generated by a submarine in turn. This includes off-body vortices (A), as well as tip vortices generated by the fin tip (B) and control surfaces (C). These separating flows contribute towards a submarines overall acoustic signature and affects its dynamics [5].

Understanding the flow physics requires a synthesis of CFD simulations and experimental measurements. This paper presents PIV measurements conducted on the DSTO hull form at side slip

angles of  $\beta = 0^\circ$  and  $\beta = 10^\circ$ . PIV is a non intrusive flow visualisation technique that can provide quantitative whole field instantaneous and time averaged velocity measurements. Measurements were conducted along the centreline of the hull at  $\beta = 0^\circ$  and multiple planes at  $\beta = 10^\circ$ . The PIV results for  $\beta = 0^\circ$  were shown to be in good agreement with Large Eddy Simulation models [1]. The study also highlighted the strengths of LES compared to Reynolds-Averaged Navier-Stokes (RANS) models in identifying detailed flow structures. This paper presents additional PIV data for future CFD validations.

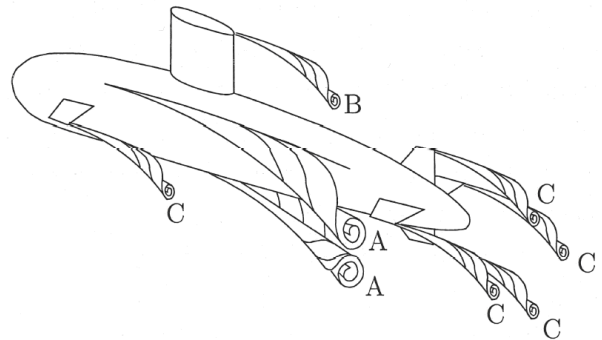


Figure 1. Schematic diagram of systems of vortices generated by a submarine in turn [12]

### Test Facility and Generic Submarine Hull form

Experiments were conducted in the DSTO LSWT. The facility is a conventional, continuous flow, closed-circuit, wind tunnel with a contraction ratio of 4:1. The test section has an irregular octagonal shape and measures 2.74 m (wide)  $\times$  2.13 m (high). The free-stream stream-wise component turbulence intensity is less than 0.4 %, and the transverse components intensities are less than 0.7 % [4]. The model length (L) and diameter (D) are 1.35 m and 0.185 m, respectively. Refer to [1] for full model details. The free-stream velocity was 30 m/s yielding a Reynolds number, based on the model length, of  $Re = 2.7 \times 10^6$ . In order to improve the PIV measurement quality, the model was black anodised to minimise surface reflections. A boundary layer trip, consisting of 3 mm carborundum grit (size 80), was used for all PIV measurements. The trip was located at 0.05L downstream from the nose of the submarine. The model was mounted to the test section via a floor-mounted pylon and shrouded by a streamlined fairing.

The field-of-view(s) was captured with respect to the upstream fin tip, downstream fin tip, at the tail and the wake region, as illustrated in Figure 2. At  $\beta = 10^\circ$  four measurement planes (MP) were captured. The field-of-view(s) were aligned with the free-stream and were with respect to the upstream fin tip (MP1), downstream fin tip (MP2), the casing-hull join (MP3) and the tail (MP4), as shown in Figure 3.

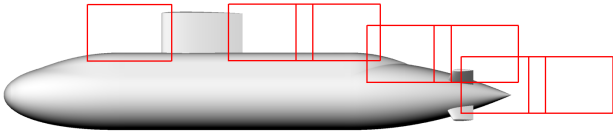


Figure 2. Locations of PIV measurement field-of-view(s) along the model centreline at  $\beta = 0^\circ$

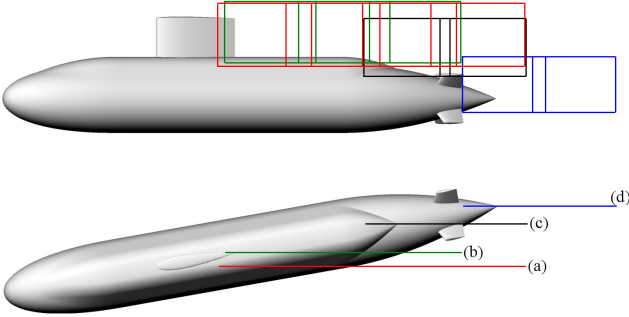


Figure 3. Locations of PIV measurement field-of-view(s) at  $\beta = 10^\circ$  (a) MP1 (b) MP2 (c) MP3 (d) MP4

### Experimental Methodology

The 2D plane of interest was illuminated using a New Wave Solo PIV 200XT Nd:YAG dual-pulse laser. The laser emits two independently controlled beams at a wavelength of 532 nm, maximum pulse energy of 200 mJ and a 5 ns pulse width. The laser was mounted above the working section on a two degree of freedom translating system, as illustrated in Figure 4. An optical train comprising a cylindrical and spherical lens was used to generate a light sheet. The laser sheet was aligned such that it was parallel to the free-stream flow direction. The laser sheet was measured to be approximately 1.5mm thick on the model surface.

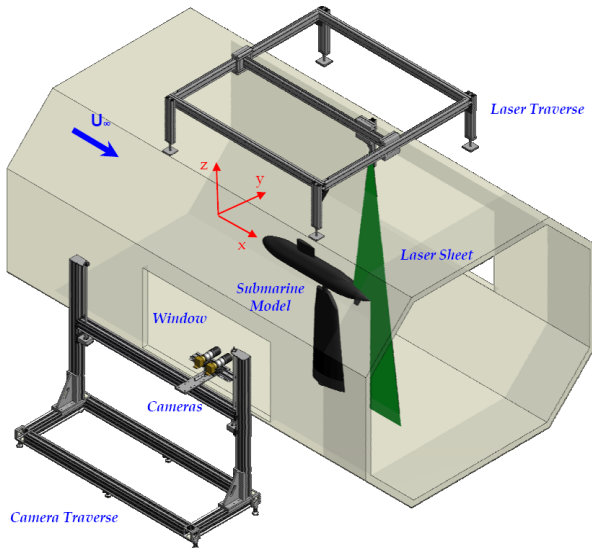


Figure 4. PIV arrangement showing model mounted in LSWT with dual cameras positioned orthogonal to laser sheet

Image acquisition was achieved using two TSI PowerView™ Plus 11 mega pixel CCD cameras, fitted with 200 mm Micro Nikkor f/4 lenses. The cameras were mounted on a three degree of freedom translating system and positioned orthogonal to the laser sheet, as shown in Figure 4. Each camera has a pixel resolution of  $4008 \times 2672$ , a pixel size of  $9 \times 9 \mu\text{m}^2$  and a frame rate of 2.07 Hz in frame straddling mode. Data acquisition and processing was conducting using TSI INSIGHT™ 4G software.

The PIV seed particles were olive oil droplets generated through a Laskin nozzle (TSI 6-jet oil droplet generator). The LSWT was

globally seeded with the oil aerosol introduced downstream of the test section. The particles have a specific gravity (SG) of approximately 0.92 and a mean droplet diameter of approximately  $1 \mu\text{m}$ , for which the particle relaxation time was calculated to be approximately  $2.4 \mu\text{s}$ . The seeding concentration was monitored via a TSI Aerosol Monitor DUSTTRAK II and a concentration of approximately  $90 \text{ mg/m}^3$  was maintained.

It is desirable to maximise the field-of-view in order to capture larger flow region in a single realisation. However, high spatial resolution is essential to adequately capture and resolve flow structures. These are conflicting requirements, as high spatial resolution results in a smaller field-of-view. This was overcome by employing a twin camera arrangement. The overlap region was set to approximately 20% and the overlapping areas of the ensemble-averaged field-of-view(s) were blended together during post-processing using the approach described in [11].

At  $\beta = 0^\circ$ , the offset distance from the centre of the test section to the PIV camera was approximately 1.6 m, resulting in a reproduction ratio of 6.7 and a spatial resolution of  $60 \mu\text{m/pixel}$ . At  $\beta = 10^\circ$ , the distance from the measurement plane to the PIV camera varied. The resulting reproduction range was between 6.2 and 7.0 and a spatial resolution range between  $56 \mu\text{m/pixel}$  and  $63 \mu\text{m/pixel}$ .

The time intervals between laser pulses was  $\Delta t = 12 \mu\text{s}$ , based on a requirement that the maximum particle displacements be less than 25% of the initial interrogation window (IW) size of  $64 \times 64$  pixels. For the image capture settings (f-stop 11 and equivalent reproduction ratio) the diffraction limited particle image diameter was estimated at 1.82 for  $\beta = 0^\circ$  and varied between 1.81 to 1.84 pixels for  $\beta = 10^\circ$ . Peak-locking was assessed by plotting histograms of particle displacement. The displacement counts were not biased towards integer pixel values indicating that peak-locking was not present. All test cases showed an acceptable distribution.

The PIV data was processed through a two-pass recursive algorithm using 50% grid spacing overlap and a first pass IW size of  $64 \times 64$  pixels. The second pass used an IW size of  $32 \times 32$  pixels. The IW was offset by the particle image displacement distance of the first processing pass. By offsetting the IW by the particle image displacement distance, lost pairs due to in-plane motion were reduced, thus increasing the signal-to-noise ratio. The resultant vector fields were validated using a global velocity range test and a median test using a neighbourhood size of  $3 \times 3$  pixels and a displacement tolerance of 2 pixels. Rejected data points were then interpolated.

### Data Convergence and Measurement Uncertainty

A running average of the velocity components and the Reynolds stresses showed that the data approached statistically stationary values with no accumulative bias error. The Reynolds stress running average stabilised after approximately 500 samples and indicated that the number of vector fields recorded for each test case was adequate in establishing sufficient convergence in the statistical parameters. Measurement uncertainty was reduced by acquiring 3000 image pairs for each field-of-view.

The measurement uncertainties in the instantaneous, mean and fluctuating velocity components were calculated using the approach described in [10]. The uncertainty of the instantaneous, mean and RMS turbulence are  $\pm 3.7 \times 10^{-3}$ ,  $\pm 0.7 \times 10^{-2}$ , and  $\pm 2.6 \times 10^{-2}$  respectively. The uncertainties in the mean and fluctuating velocity components are based on random variable analysis for 95% confidence interval. The transverse velocity (v) component is assumed to have an identical uncertainty as the stream-wise velocity (u) component.

## Results and Discussion

The results are presented in model scale, with the origin located at the nose of the submarine model. Figure 5 presents the non-dimensional stream-wise velocity, transverse velocity and RMS turbulence intensity on the model symmetry plane at  $\beta = 0^\circ$ . Upstream of the fin the stream-wise velocity is initially uniform, with the boundary layer increasing in thickness as it approaches the leading edge of the fin. The transverse velocity shows the flow to be accelerating over the casing and leading edge fin tip. In front of the base of the fin, the flow is expected to roll into a horse-shoe vortex system and sweep around the fin [1]. The cross-section of the horse-shoe structure is evident in Figure 5 (a) which shows a magnified view near the leading edge casing-fin junction. The figure presents the positive contours of the second invariant of the velocity gradient tensor,

$$Q = (\Omega_{ij}\Omega_{ij} - S_{ij}S_{ij})/2, \quad (1)$$

where  $S_{ij} = (u_{i,j} + u_{j,i})/2$  and  $\Omega_{ij} = (u_{i,j} - u_{j,i})/2$  are the rate-of-strain and rate-of-rotation tensor, respectively and  $u_{i,j}$  is the velocity gradient tensor. By assuming the flow is symmetric about the model centreline ( $x$ - $z$  plane)  $Q$  was derived using only the in-plane velocity gradients; derivatives with respect to  $z$  and all derivatives of the mean out-of-plane velocity  $\bar{W}$  are zero on the  $x$ - $z$  plane. Also plotted are streamlines derived from an integration of the velocity field in a local frame of reference (derived by subtracting the velocity components near the centre of the horseshoe vortex, as identified by the contours of  $Q$ ). The streamlines spiral towards a stable focus where, due to mass conservation arguments, the fluid is ejected normal to the plane and develops the horse-shoe structure.

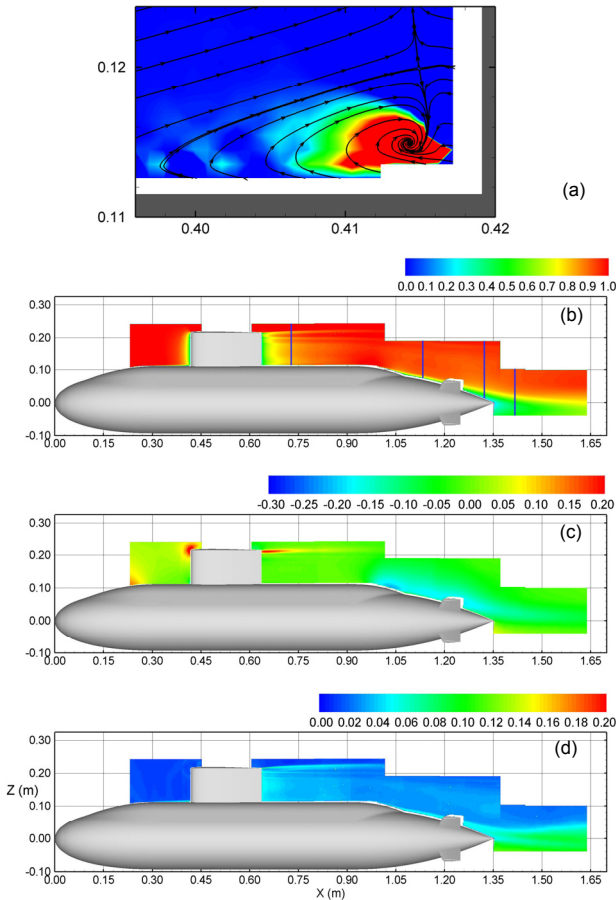


Figure 5. Ensemble-averaged non-dimensional (a) Contours of  $Q$  overlaid with streamlines near the casing-fin junction (b) stream-wise velocity (c) transverse velocity, and (d) RMS turbulence intensity

Downstream, the wake shows a velocity deficit across the fin wake with associated higher turbulence intensity in this region. Also evident are two stream-wise structures which extend downstream from the fin tip, shown in Figure 5 (d). These can be attributed to the primary (upper) and secondary (lower) vortices shed from the fin. Profiles of the averaged stream-wise velocities, at four downstream locations indicated in Figure 5 (b), are presented in Figure 6. In Figure 6 (a) the tip vortices are evident as local minima in the velocity with the primary and secondary vortex positioned above and below the fin tip location (of  $Z = 0.21$  m). Further downstream the flow accelerates over the casing-body aft-end junction and is followed by a rapid growth in the boundary layer, shown in Figure 5 (c). There is, however, no evidence of flow separation in the mean velocity field. Downstream of the model, the RMS turbulence intensity shows an asymmetric distribution about the model centreline, with higher values for  $Z < 0$ , as evident in the profiles shown in Figure 6 (d). Support fairing interference effects and the associated unsteady wake may be a contributor to the regions higher turbulence levels.

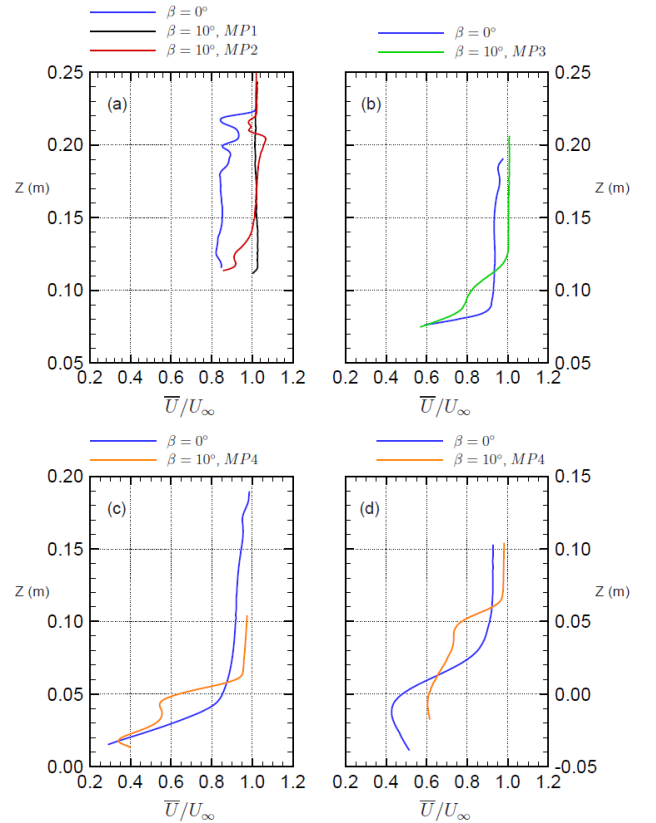


Figure 6. Ensemble-averaged streamwise velocity profiles at (a)  $x/L=0.54$ , (b)  $x/L=0.84$ , (c)  $x/L=0.98$  and (d)  $x/L=1.05$

The non-dimensional stream-wise and transverse velocity for the four  $\beta = 10^\circ$  measurements planes are presented in Figure 7. The figures represent a stream-wise slice through the fin leading edge (MP1) and trailing edge (MP2) respectively (as defined in Figure 3). At these locations the transverse velocity in the vortex core is shown to be negative at MP1 and positive at MP2, as shown in Figure 7 (b). This is consistent with the radial velocity expected from the tip vortex. Preliminary comparisons with RANS-based CFD simulations have confirmed this [13].

The tip structure extends the length of the model and curves gradually downwards. The stream-wise velocity through MP1 is relatively uniform, while at MP2 a wake deficit is observed downstream of the fin. The velocity profile presented in Figure 6 (a) for MP2 shows a peak in the axial velocity that exceeds the free-stream velocity.

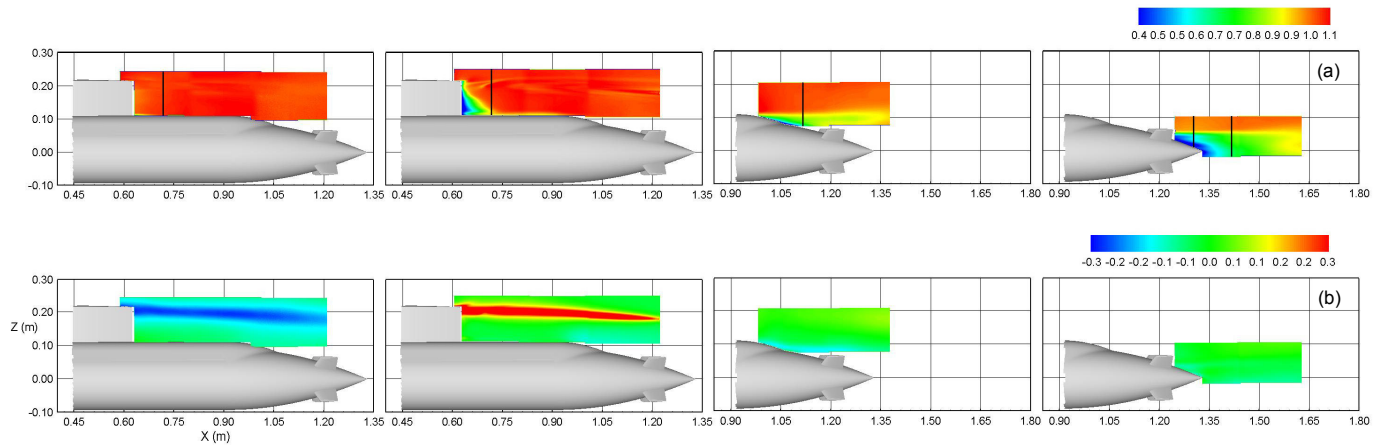


Figure 7. Ensemble-averaged non dimensional (a) stream-wise velocity, and (b) transverse velocity. Measurement planes MP1 to MP4 are shown from left to right

Studies on the flow over wing tips at incidence have shown that the streamwise velocity through the vortex core can be significantly higher than the free-stream velocity [2, 3]. The velocity increase near the tip vortex location is consistent with the earlier studies. Over the casing-hull (MP3) and the hull trailing edge (MP4), the stream-wise flow shows a rapid growth in the boundary layer and a broad wake region which is associated with the cross-stream flow. In Figure 6 (b) and Figure 6 (c) the impact of the cross-stream flow is demonstrated by the greater velocity deficit (when compared to  $\beta = 0^\circ$ ) for both measurement planes.

The current dataset has focused on PIV measurements along the length of the DSTO hull form. These measurements do not enable the appreciation of the size and location of various vortical systems. Future studies will focus on conducting cross-stream Stereo Particle Image Velocimetry (SPIV) measurements. These measurements will provide insights into the evolution of vortex core size as well as identify potential locations of cross-body separation.

## Conclusions

PIV measurements were conducted on the DSTO hull form at side slip angles of  $\beta = 0^\circ$  and  $\beta = 10^\circ$ . At  $\beta = 0^\circ$ , the horse-shoe vortex at the leading edge casing-fin junction was identified as well as the primary and secondary fin tip vortices. At  $\beta = 10^\circ$ , the positive and negative transverse velocities of the fin tip vortex core was captured. The PIV measurements, in conjunction with other experimental results, will provide insight into the vortical systems generated around a submarine. This experimental database will be referred to for future CFD validation.

## Acknowledgments

The assistance of the following people during the course of this work is acknowledged; Brendon Anderson, Bruce Woodyatt, Paul Jacquemin, Dr Ronny Widjaja and Kate Bourne.

## References

[1] Anderson, B., Chapuis, M., Erm, L., Fureby, C., Giacobello, M., Henbest, S., Jones, D., Jones, M., Kumar, C., Liefvendahl, M., Manovski, P., Norrison, D., Quick, H., Snowden, A., Valiyff, A., Widjaja, R. & Woodyatt, B., Experimental and Computational Investigation of a Generic Conventional Submarine Hull Form, in *29th Symposium on Naval Hydrodynamics*, 2012: Gothenburg, Sweden.

[2] Chigier, N.A., & Corsiglia, V. R., Tip Vortices-Velocity Distributions, 1971, NASA TM X-62087.

[3] Chow, J.S., G.G. Zilliac, and P. Bradshaw, Mean and turbulence measurements in the near field of a wingtip vortex. *AIAA journal*, 1997. **35**(10): p. 1561-1567.

[4] Erm, L.P., Calibration of the Flow in the Extended Test Section of the Low-Speed Wind Tunnel at DSTO, DSTO Report DSTO-TR-1384, 2003, DSTO Melbourne, Australia.

[5] Gregory, P., Flow over a Body of Revolution in a Steady Turn, Doctor of Philosophy, 2006, University of Melbourne, Melbourne, Australia.

[6] Groves, N.C., Huant, T.T., & Chang, M.S., Geometric Characteristics of DARPA (Defense Advanced Research Projects Agency) SUBOFF Models (DTRC Model Numbers 5470 and 5471), DTRC/SHD-1298-01, 1989, David Taylor Research Center, Bethesda, Maryland 20084-5000.

[7] Huang, T.T., Liu, H.L., & Groves, N.C., Experiments of the DARPA SUBOFF Program, DTRC/SHD-1298-02, 1989, David Taylor Research Center, Bethesda, Maryland 20084-5000.

[8] Joubert, P.N., Some Aspects of Submarine Design Part 1 – Hydrodynamics, DSTO Report DSTO-TR-1622, 2004, DSTO Melbourne, Australia.

[9] Joubert, P.N., Some Aspects of Submarine Design Part 2 – Shape of a Submarine 2026, DSTO Report DSTO-TR-1920, 2006, DSTO Melbourne, Australia.

[10] Kostas, J., An experimental Investigation of the Structure of a Turbulent Backward Facing Step Flow, Doctor of Philosophy, 2002, Monash University, Melbourne, Australia.

[11] Kumar, C., Widjaja, R., Giacobello, M., & Manovski, P., PIV Image Stitching using MATLAB, DSTO Report in preparation, 2012, DSTO Melbourne, Australia.

[12] Lloyd, A.R.J.M., & Campbell, I.M.C., Experiments to investigate the vortices shed from a submarine-like body of revolution, in *59th meeting of the AGARD Fluid Dynamics Symposium 1986*: Monterey, California.

[13] Widjaja, R., Private Communication, Aug. 2012.